Available online at www.sciencedirect.com
ScienceDirect
International Journal of Solids and Structures 44 (2007) 145–164
INTERNATIONAL JOURNAL OF SOLIDS and STRUCTURES
www.elsevier.com/locate/ijsolstr

Viscoplastic parameter estimation by high strain-rate experiments and inverse modelling – Speckle measurements and high-speed photography

Jörgen Kajberg *, Bengt Wikman

Division of Solid Mechanics, Luleå University of Technology, SE-97187 Luleå, Sweden

Received 16 August 2005; received in revised form 4 April 2006
Available online 26 April 2006

Abstract

A methodology based on inverse modelling for estimating viscoplastic material parameters at high strain-rate conditions is presented. The methodology is demonstrated for a mild steel exposed for compression loading in a split Hopkinson pressure bar arrangement. By using dog-bone shaped specimens nonhomogeneous states of deformation are obtained throughout the entire deformation process. The resulting nonhomogeneous deformation of the specimens is evaluated using digital speckle photography (DSP) to give in-plane point-wise displacement and strain fields. The photographs are captured with a high-speed camera of image converter type, which acquire time resolved images during the impact loading. The experiments are simulated using finite element analysis (FEA), where the material model suggested by Johnson–Cook for high-strain rate conditions are utilised. Experimental and FE-calculated field information are compared in order to estimate the viscoplastic parameter in the Johnson–Cook material model. The estimation is performed by minimising least-square functions that contain the differences in displacements and strains, respectively. The quality of the estimated parameters is studied from statistical point of view.

Keywords: Constitutive behaviour; Viscoplastic material; Split Hopkinson bar; Digital speckle photography (DSP); High-speed photography; Inverse modelling

1. Introduction

Stresses due to inelastic deformation of materials are generally sensitive to the rate of strain. The rate sensitivity of the flow stress can be demonstrated in the low rate domain on commonly used tensile testing machines by changing the crosshead velocity. Knowledge of the rate sensitivity is necessary for calculations and simulations of for example manufacturing processes, such as plastic forming and cutting etc. Accurate information of the mechanical properties of materials at strain rates exceeding the rates attainable on commonly used testing machines are necessary for such simulations.

* Corresponding author. Tel.: +46 920 491284; fax: +46 920 491047.
E-mail addresses: Jorgen.Kajberg@bredband.net (J. Kajberg), b_wikman@hotmail.com (B. Wikman).

0020-7683/$ - see front matter
doi:10.1016/j.ijsolstr.2006.04.018

The mechanical behaviour of materials subjected to high strain rates is described by viscoplastic constitutive models. Such models have been suggested by for example Perzyna (1963), Johnson and Cook (1983). These models are all purely empirical, while other models are more physically based (Zerilli and Armstrong, 1987; Follansbee and Kocks, 1988; Nemat-Nasser and Kapoor, 2001). All these models contain material parameters, which are not well known for higher strain rates. For reviews of the area of viscoplastic modelling see for example Lemaitre and Chaboche (1990), Meyers (1994), Liang and Khan (1999).

The experimental technique called split Hopkinson pressure bar (or Kolsky bar) (Kolsky, 1949; Gray III, 2000) is commonly used for material parameter estimation in high-rate viscoplastic models. Typical strain rates achieved with the split Hopkinson pressure bar arrangement are of magnitude $10^3\ s^{-1}$. The Hopkinson bar is generally designed to achieve a uniform stress and strain condition as well as force equilibrium in the specimen. This allows direct evaluation of the stress–strain relation at a certain strain rate. However, the deformation regime in which the specimen is loaded dynamically such that the whole gauge section is deformed homogeneously is difficult to achieve when sound speed is low in the specimen, which is typical for some polymeric materials (Walley and Field, 1994). In addition the stress uniformity is opposed by inertia and by frictional forces at the specimen–pressure bar interface. Further, the true stress and strain cannot be extracted for materials whose volumes are not conserved. Materials for which this problem occurs include metallic and polymeric foams, honeycomb structures and porous compacts, which all exhibit a volume change during mechanical loading. In these situations additional sample diagnostics are required for monitoring the deformation of the specimen that can provide the needed data to calculate the true stress and strain. For example a high-speed camera can be used in such situations. In some recent papers high-speed photography has been utilised for deformation measurements of steel specimens subjected to stress triaxiality (Hopperstad et al., 2003; Kajberg et al., 2004).

In this paper the outline for a combined experimental/numerical methodology for material parameter estimation is presented where neither uniform stress and strain nor force equilibrium are required. The methodology is demonstrated for characterisation of a mild steel.

A split Hopkinson pressure bar arrangement is still used for loading and force measurements, but the resulting displacement field on the surface of the specimen is evaluated by digital speckle photography (DSP) using a high-speed camera. DSP has been applied for full-field displacement measurement in many applications, e.g. Wattrisse et al. (2001), Jernkvist and Thuvander (2003), and Molin et al. (2004). However, the combination of a high-speed camera and DSP in high-strain rate experiments has been used, to the authors' knowledge, only in Grantham et al. (2003) and Kajberg and Sjödahl (2003).

In order to estimate constitutive parameters in a viscoplastic model inverse modelling (Tarantola, 1987) is used. The basic approach in inverse modelling is to employ a so-called objective function that measures the agreement between the experimental data and the model with a particular choice of parameters. The application of inverse modelling is presented in for example Mahnken and Stein (1994) and Kajberg et al. (2004).

In this paper, the chosen constitutive model is the one suggested by Johnson and Cook (1983). The model is employed in a finite element (FE) program and the rapid loading of the specimens are simulated. Further, the objective function is based on the difference between field information from the FE-calculation and the experiment.

The parameters of the model are then adjusted to achieve a minimum in the objective function, yielding best-fit parameters. In this case a least-square fit is achieved. The adjustment process is thus a problem of optimisation in many dimensions. Using this method will in most cases provide a set of optimal parameters. However, the quality of the estimated parameters should also be analysed. Since experimental data are generally not exact, they are associated with measurement errors. Typically, the model that is being used never exactly fits the experimental data.

The existence of a minimum for the objective function must be considered, i.e. appropriate requirements on the gradient and the curvature of the objective function must be posed. The function may not be unimodal and several optima may coexist. Another crucial issue to investigate is the stability of the achieved solution (Baumeister, 1987). For instance, a flat minimum is considered nonunique, and for this reason the solution may change substantially by even small changes in the data. It is also common practice to summarise the distribution of errors in the estimated parameters by a confidence interval. That is, an interval for which one can assert with a given probability that it will contain the parameters it is intended to estimate. Finally, it is necessary to

assess whether the model is appropriate or not. Hence, there is a need to test the goodness-of-fit against some useful statistical standard (Kleinbaum and Kupper, 1978).

The current experiments provide strain rates of magnitude 10^2–10^3 s^{-1}. Thus, the region of validity for the estimation is limited to this interval. The work presented in this paper primarily emphasizes the methodology for determining material parameters using high strain rate experiments, digital speckle photography and inverse modelling techniques. A similar approach, where the methodology is utilised, is characterisation of materials subjected to large strains under static conditions, which is described in Kajberg and Lindkvist (2004).

2. Experiments

The deformation process of a material can often be divided in an elastic part and a plastic part. When the deformation becomes plastic, hardening effects might occur. The hardening of a material can be described by strain hardening and viscoplastic hardening. Viscoplasticity implies a strain rate dependency, which for many metals becomes significant when the strain rate exceeds 10^2 s^{-1}. The strain hardening is easily obtained by subjecting the material to static loading in a common tension and compression testing machine. The characterisation of the viscoplastic hardening, on the other hand, requires a method providing dynamically loaded material samples. In this study the dynamic tests are performed by using the Split Hopkinson Bar arrangement.

2.1. Set-up and specimen type for the dynamic tests

The split Hopkinson pressure bar is shown in Fig. 1. The bars are made of quenched steel with yield stress of about 500 MPa and have diameters of 25 mm. The lengths of the bars are 1.5 m and 1.45 m for the incident bar and the transmitter bar, respectively. Hence the length-to-diameter ratio is 60 and one-dimensional wave propagation is thereby ensured (Gray III, 2000).

The compressive loading is achieved by using a projectile of the same material and diameter as the bars. The projectile is accelerated inside an air gun and impacts the end of the incident bar.

In classic split Hopkinson pressure bar testing a rectangular shape of the incoming wave is desirable for achieving an approximately constant value of the strain rate. By using a projectile of the same material and diameter as the incident bar, and by attaching a so-called pulse shaper at the impact end of the incident bar, a nearly rectangular shape is achieved. A pulse shaper is a thin washer of a softer material that damps the impact slightly and thus counteracts dispersive effects such as overshoots, which would appear in the incoming wave if the projectile impacts the incident bar directly. A smooth rectangular incoming wave is here utilised by using an aluminium shim as a pulse shaper.

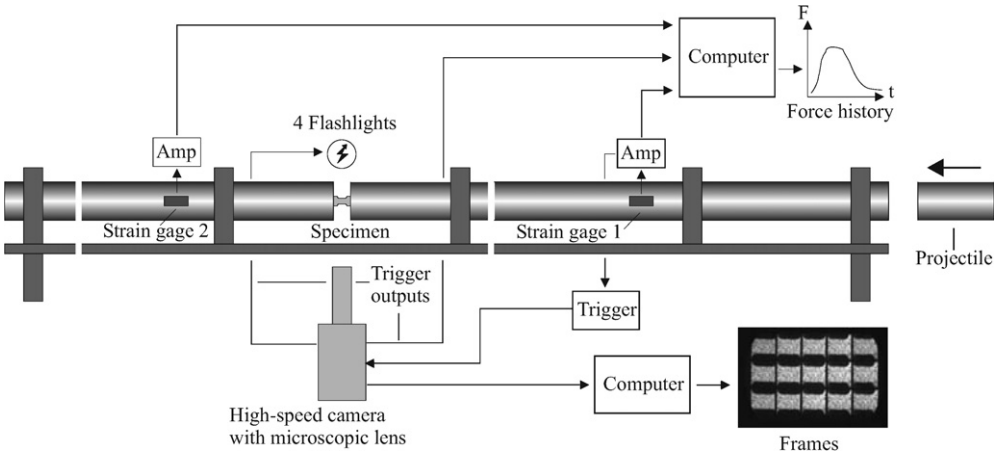

Fig. 1. Split Hopkinson pressure bar arrangement complemented with a high-speed camera.

The incoming wave and also the reflected wave are measured with one pair of strain gauges, which are mounted on the incident bar. The portion of the wave that is transmitted through the specimen is measured with one pair of gauges on the transmitter bar. All strain gauges (Measurements group CEA-06-250UW-350) are of foil type with a gauge length of 6.35 mm. The signals from the gauges pass through the amplifiers (Measurements group 2210A) with bandwidths of 100 kHz and are finally sampled with a frequency of 2 MHz. With steel bars and a strain gauge length of 6.35 mm the time resolution of the wave measurements is limited to approximately 1 μs. This is assumed to be sufficient for resolving the rise times in this specific case.

The common way to determine the input and output force in a split Hopkinson bar arrangement is by time-shifting the incoming, reflected and transmitted elastic waves so they coincide with the specimen interfaces. The input force F_{in} is then calculated by adding the incoming and reflected wave, and the output force F_{out} is determined by considering the transmitted wave. More details concerning the force evaluation could be found in Gray III (2000).

Furthermore, one of the strain gauges on the incident bar is connected to a "trigger box" which sends a trigger signal to the high-speed camera when the strain reaches a certain level. The specimen is illuminated by four flashlights whose risetimes must be considered for achieving maximum irradiance. They are therefore activated 100 μs before the compression wave reaches the specimen.

The high-speed camera that is used (ULTRANAC FS 501) is of image converter type with a CCD-unit (charged coupled device). The CCD-unit provides a captured image with fixed spatial resolution. Further, the image can be divided in different arrays of frames. The maximum number of frames, which is possible to capture, consists of an array with up to 4×6 frames. The disadvantage with this frame configuration is that the lowest spatial resolution of the frames is provided. As a compromise between number of frames and a good spatial resolution, the configuration with 3×5 frames is chosen in the presented experiments. The exposure time and the interframe period are set to 2 μs and 8 μs, respectively. The exposure time is kept as short as possible without risking the necessary illuminance and to avoid blurring caused by the motion.

The design of the mild steel (SS 141672) specimens used in the tests is shown in Fig. 2. The specimens are machined with narrow sections in the middle for providing nonhomogeneous stress and strain states. The manufacturing method is electric wire discharge, which is assumed to have only a small influence on the machined surfaces. In order to receive low-friction specimen–bar interfaces silicone oil is applied. Three specimens, denoted no. 1, 2 and 3, are used. Note the definition of coordinate system (Fig. 2) that is used throughout this paper.

2.2. Displacement and strain measurement using speckle photography

Fig. 3 shows a captured sequence of frames of a deforming specimen. By using digital speckle photography (DSP) the displacement from the initial to the current position could be determined for any material point on the specimen surface. So by representing the specimen surface with a large set of material points an in-plane displacement field is obtained. Strain field information could then be evaluated through some proper filtering method and differentiation.

The most fundamental requirement for the DSP-method, that there exists a random pattern at the object surface, is accomplished by using diffusely reflecting black and white spray paint (see Fig. 3). The randomness

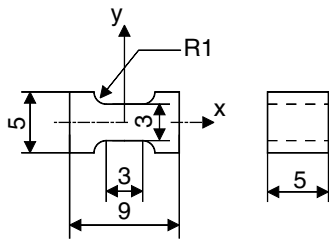

Fig. 2. Specimen. All dimensions are in mm.

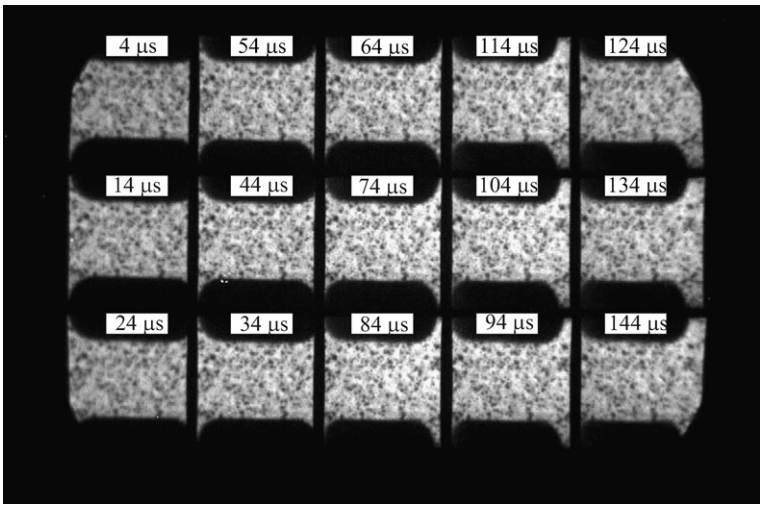

Fig. 3. A sequence of captured frames of a deforming specimen. The time information indicate elapsed time after arrival of the compression wave. The frames show an area of approximately $4.6 \times 5.3\ \text{mm}^2$.

ensures that any small region of the object surface is unique. By capturing the object surface with a digital camera before and after the object has been subjected to some kind of displacement or deformation any small unique region can be tracked by using a cross-correlation algorithm (Sjödahl, 1994). In order to get field data, the object surface is divided into a large number of such small unique regions, so-called subimages. The cross-correlation algorithm can be described schematically by dividing it into three steps. Firstly, a rough estimation of the displacement components is performed with a precision of half a pixel. That is, the components are given integer values. Secondly, based on these estimated components a new subimage belonging to the deformed object surface is selected and noninteger values of the displacement components are obtained. Thirdly, the accuracies of the obtained noninteger values are improved by using a shift technique based on Fourier series expansion. Hence the shift technique counteracts cross-correlation of nonoverlapping regions of subimages and more accurate and reliable speckle displacements are thereby obtained.

In this specific case, the high-speed frames showing the object surface, consist of 166×192 pixels and the sizes of the subimages are set to 32×32 pixels. The midpoints of the subimages are separated by 8 pixels in both x- and y-direction and therefore the subimages overlap each other with the ratio 24/32. The separation defines the spatial resolution of the evaluated displacement field, which in this case has a size of 17×21 points.

A problem with a high-speed camera of image converter type is that aberrations are introduced in the imaging. Different parts of the image therefore render the captured object at slightly different scales. A calibration procedure is therefore introduced for relating evaluated displacements to physical displacements on the object. It involves comparison of frames taken of a stationary pattern at instants with known rigid displacements and is described in detail in Kajberg and Sjödahl (2003).

The evaluation of the in-plane true strain/shear components ε_x, ε_y and ε_{xy} by using the first-order Savitsky–Golay filter (Press et al., 1992) is described in detail in Kajberg and Lindkvist (2004). The shear component is not used in the following inverse modelling.

2.3. Uncertainties

It is of importance to estimate the uncertainties of the displacement quantities u and v (x- and y-direction) and the strain quantities ε_x and ε_y, since they are the basis for subsequent estimation of material parameters. In this paper, their standard deviations are used as the estimation of their uncertainties. The standard deviations depend of the regression model used for strain evaluation, the correlation values from the DSP-calculations and the size of the speckles. As a measure of the speckle size the radius of the correlation peak is used (Sjödahl, 1997). The uncertainty analysis is presented in detail in Kajberg and Lindkvist (2004), resulting in uncertainties given by

$$\begin{pmatrix} s_u = s_v \\ s_{\varepsilon_x} = s_{\varepsilon_y} \end{pmatrix} = \begin{pmatrix} 0.3333 \\ 0.0510 \end{pmatrix} 0.7 \frac{\sigma^2}{B} \sqrt{\frac{1-c}{c}} \tag{1}$$

where $B = 32$ pixels is the size of the subimages, c are the correlation values and σ are the radii of the correlation peaks.

2.4. Static tests

In order to obtain the strain hardening under static conditions compression tests (ASTM Standard E9-89a, 1995) are performed in a common tension and compression testing machine, DARTEC M1000 (250 kN) with control unit M9500. Three tests are performed at a strain rate of $\dot{\varepsilon}_0 = 5.7 \times 10^{-3}\ \mathrm{s}^{-1}$. The specimens are cylinders with diameter and a length of 12 mm and 36 mm, respectively.

3. Experimental results

3.1. Forces

The force histories measured with the strain gauges mounted on each Hopkinson bar are presented for specimen no. 1 in Fig. 4. Further, the evaluated input and output forces for this specimen are presented in Fig. 5. The third curve, output force $F_{\mathrm{out}}^{\mathrm{FE}}$, will be discussed later. The time scales shown in the graphs are zero when the pulse reaches the specimen interface. At times marked with stars displacement and strain fields are evaluated and at times marked with circles photos are taken but fields are not evaluated due to too small or too large speckle displacement.

An inspection of Fig. 5 shows that the input and output force have the same general appearance, which could be expected since inertia forces are small. Further, the incoming wave in Fig. 4 shows a small amount of oscillations. However, no dispersion correction is performed since the oscillations are considered to be small and thereby not invalidating accurate force measurement.

3.2. Displacements and strains

One component of the evaluated strain fields for specimen no. 1 is presented in the left pictures in Fig. 12 as filled level curves on the captured area of the specimens. The region chosen for evaluation of strain fields is limited to the narrow part of the specimen.

With the correlation algorithm used in the evaluation of speckle displacement, the maximum detectable displacement is set to 24 pixels. It should be mentioned that the largest displacement determined is 21 pixels. The

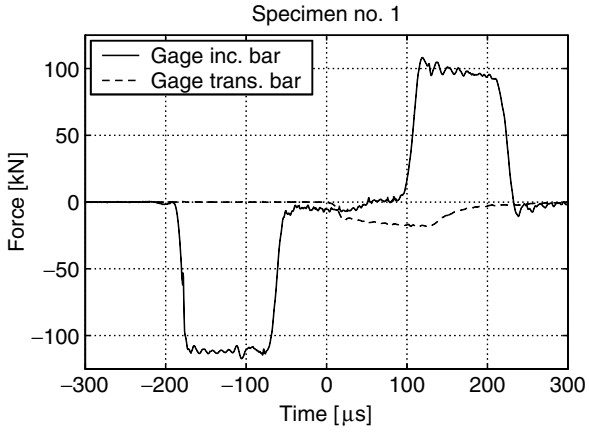

Fig. 4. Force histories for specimen no. 1 at the gauge positions in the incident and transmitter bar evaluated from the strain gauge data.

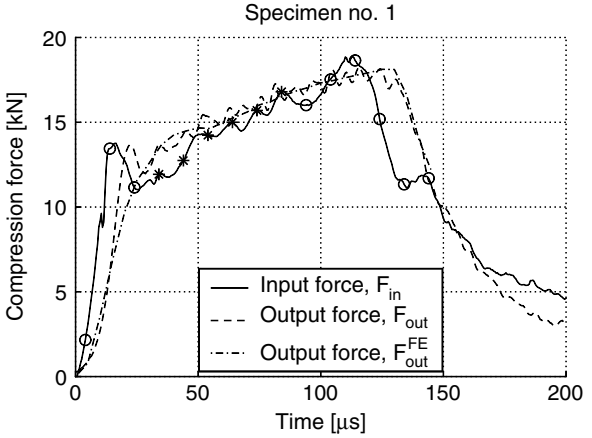

Fig. 5. Input and output forces for specimen no. 1. Stars and circles mark times when photographs are taken.

reasonable explanation why not larger values could be detected is that large displacements, in this specific case, are subjected to high strain values causing poor speckle correlation. Here, poor correlation values mean values below 0.7. The evaluated displacements corresponding to these correlation values are therefore considered as unreliable.

In the evaluations of the strain fields the first three and last three frames have always been excluded due to bad sharpness along the short sides of the captured image. This bad sharpness appears independent of choice of frame configuration. With some patience, it is possible to see in Fig. 3 the difference in sharpness between the frames along the short sides and the 9 frames in the middle. The configuration with 3×5 frames, chosen in this experiment, is therefore a compromise between the number of frames for evaluation and the spatial resolution which decreases with increasing number of frames.

In order to complete the uncertainty estimation according to Eq. (1), the correlation values c are needed. These values varied between 0.8 and 0.9. The higher value, 0.9, was obtained in the field evaluation for earlier times while the lower value appeared for later times. The reason for the decrease in correlation value is that the subimages become more strained for the later times. The interval for the uncertainties of the measured quantities are presented in Table 1, where the uncertainty of displacement is given in both pixels and μm. In order to calculate the uncertainties in μm the scale of the captured image has to be used. This scale is approximately 27.8 μm/pixel. The lower values in the table correspond to the earlier times. It should be underlined that the uncertainties of the strain measurement are of the same order of magnitude as the measured strains. The obtained speckle size, namely six pixels, is three times larger than the optimum size of two pixels (Sjödahl and Benckert, 1994). If it were possible to achieve the optimum size of speckles, the accuracy would improve nine times.

Other interesting quantities to estimate are the strain rates. Due to the low time resolution of about 10 μs the estimations are restricted to the midpoints of the specimens and they should be considered as indications of the achieved strain-rate levels. One simple way to estimate these strain rates is to fit straight lines to the strain data. The strain rates are then estimated by the slopes of the lines. These strain rates corresponding to the loading direction are presented in Table 2 and the development of the strains evaluated at the midpoints for all specimens is presented in Fig. 6.

Table 1
Uncertainties for the measured quantities

$s_u = s_u$	0.088–0.13 pixels $\Longleftrightarrow$ 2.4–3.6 μm
$s_{\varepsilon_x} = s_{\varepsilon_y}$	0.013–0.020 strain

Table 2
Estimated strain rates in the loading direction for the midpoint of the specimens

Specimen	1	2	3
Strain rate [s^{-1}]	−1100	−1300	−1100

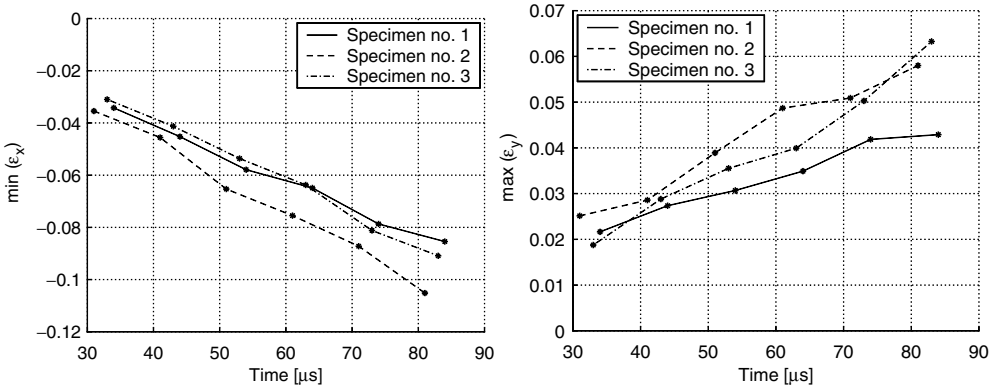

Fig. 6. Development of strains for the midpoints of the specimens.

4. Constitutive model

In order to characterise the viscoplastic behaviour the model suggested by Johnson and Cook (1983) is chosen. This model is commonly used to describe viscoplasticity, especially for strain rates up to $10^4\ s^{-1}$. The model has five material parameters, where one parameter is used to characterise the strain-rate behaviour. The effective stress σ_e according to von Mises in the Johnson–Cook model is described by

$$\sigma_e = (A + B\varepsilon_{ep}^n)(1 + C\ln\dot{\varepsilon}_{ep}^*)(1 - T^{*m}) \tag{2}$$

where ε_{ep} is the equivalent plastic strain, $\dot{\varepsilon}_{ep}^* = \dot{\varepsilon}_{ep}/\dot{\varepsilon}_0$ is the dimensionless plastic strain rate and T^* is the homologous temperature. The five material constants are A, B, n, C and m. The effect on the material properties caused by the temperature rise due to adiabatic heating is here assumed to be of less significance for this specific material, SS 141672. Thus, the last factor in the constitutive relationship is neglected. This simplified version of Johnson–Cook model is also available in the chosen FE-code, LS-Dyna. The response of omitting thermal effects in the constitutive model is checked after the parameter estimation is performed. The response is discussed in Section 8.

Since the last factor is neglected the effective stress σ_e is a product of the strain hardening factor $\sigma^{stat} = (A + B\varepsilon_{ep}^n)$ and the viscoplastic part $(1 + C\ln\dot{\varepsilon}_{ep}^*)$. The parameters A, B and n are determined by using the results from the static compression tests, in which the imposed strain rate is denoted $\dot{\varepsilon}_0$. The parameter A is the static yield stress and is estimated to $R_{p0.2}$ by the offset method (ASTM Standard E9-89a, 1995). The other two parameters B and n are determined by minimising the difference between the strain hardening factor σ^{stat} and stress–strain data obtained in the static tests in a least square sense.

The remaining parameter C that controls the viscoplastic hardening is determined by inverse modelling based on the field information from the dynamic tests.

5. Estimation of strain hardening parameters from static tests

The parameters B and n, which control the strain hardening behaviour in the constitutive model are estimated by fitting the strain hardening factor σ^{stat} to the experimentally determined static stress–strain curves. The curve fitting results in optimisation problem of a so-called objective function according to

$$\min_{B,n\in\mathbb{R}^1} \Phi(B,n) \tag{3}$$

subjected to

$$B, n \geqslant 0,$$

where

$$\Phi = \frac{1}{IJ-2}\sum_{j=1}^{J}\sum_{i=1}^{I}[\sigma_j^{\exp}(\varepsilon_{\mathrm{ep}}^i) - \sigma^{\mathrm{stat}}(\varepsilon_{\mathrm{ep}}^i)]^2 \tag{4}$$

where $\sigma_j^{\exp}$ is the jth experimentally determined true stress as a function of equispaced true strain values $\varepsilon_{\mathrm{ep}}^i$. The total number of equispaced strain values I was 121 in the compression tests. The total number of tests is denoted J and is equal to three. The denominator $IJ-2$ in Eq. (4) equals the total number of degrees of freedom.

Due to the exponential form of σ^{stat} the optimisation of Φ is nonlinear. The minimum of Φ is found by using an iterative search algorithm called the Nelder and Mead simplex method (1965), which is a built-in function in Matlab 6.5.

6. Inverse modelling

The numerical modelling of the dynamic experiments is based on FE calculations. Estimation of constitutive parameters is carried out through the solution of an inverse problem. The parameters are estimated by minimising the so-called objective function. In this specific case the objective function is based on the difference between the data from the experiments and the computed model responses and only one parameter C [see Eq. (2)] is estimated by inverse modelling.

The inverse modelling procedure can be summarised by the following steps:

- FE discretisation,
- choice of constitutive model,
- application of boundary conditions and compression loads,
- interpolation of numerical field information to coincide in space with the experimental field information,
- choice of the objective function to be minimised,
- choice of optimisation method used for solving the inverse problem.

6.1. Finite element modelling

The FE-problem is solved using LS-Dyna, which is a general-purpose, explicit finite element computer program for analysing the nonlinear dynamic response of three-dimensional inelastic structures. The dynamic test is modelled by discretisations of the specimen and the Hopkinson transmitter bar by means of eight node hexahedron solid elements, which can be seen in Fig. 7. Due to symmetry only one-quarter of the bar and the specimen is discretisised. The symmetry is however lost at the onset of specimen failure. But since the parameter estimation is based on captured images before that event the one-quarter FE-model is assumed to be sufficiently accurate.

The input load F_{in} is depicted in Fig. 5. The contact between the two parts is modelled by a frictionless sliding contact surface interface.

6.2. Interpolation of numerical field information

The DSP-algorithm used in the experiments for displacement and strain evaluation results in point-wise field information consisting of a uniform grid of values, i.e. the data points are equispaced in both directions, horizontal and vertical. However, the displacement and strain data in the FE-calculation are restricted to the nodes and the integration points, respectively. In order to compare experimental data with numerical data the FE-results are interpolated to points that coincide with the points in the uniform grid of the experiment.

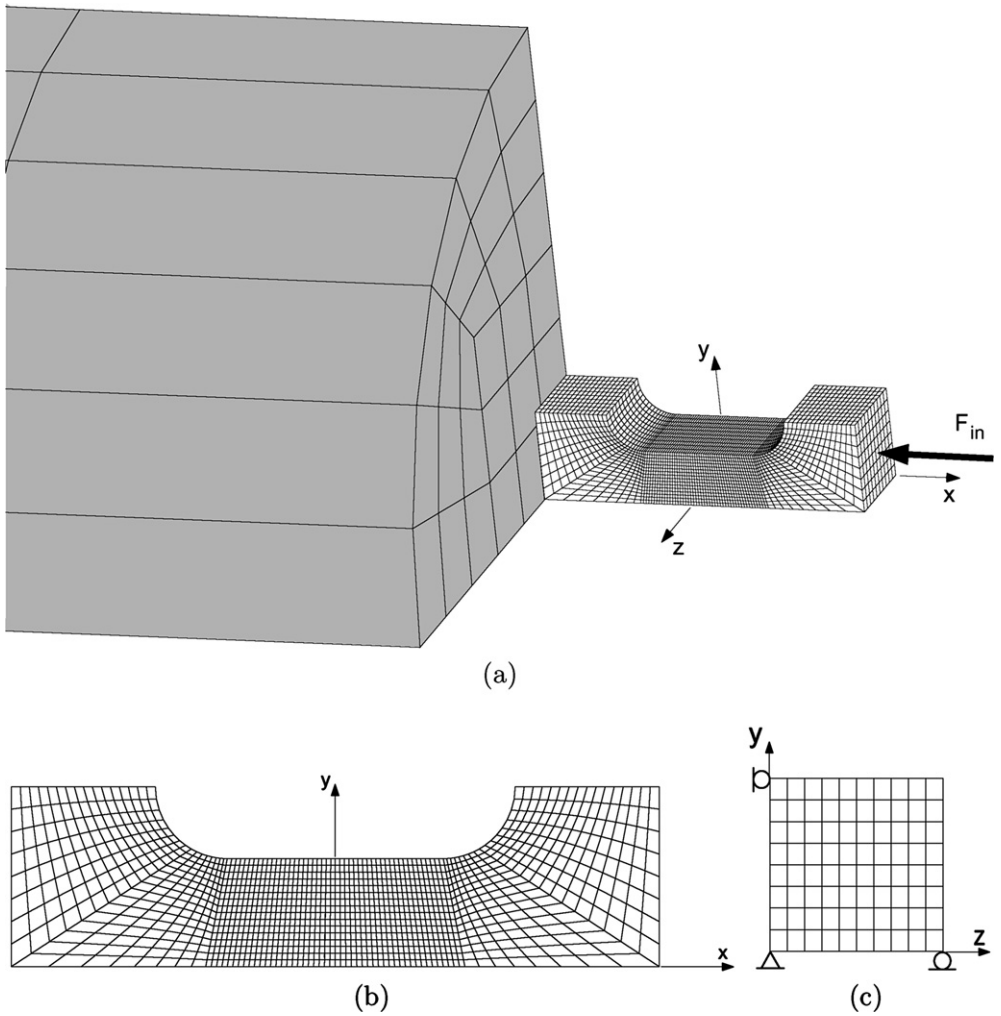

Fig. 7. FE-mesh containing the specimen and the transmitter bar (a). The specimen (b). The specimen with its applied boundary conditions shown in the loading direction (c).

The numerical values at the grid points are determined by linear interpolation between the values of the three closest nodes/integration points. In other words, all grid points lie in triangular regions, where the nodes/integration points are the apex points. These triangular regions are determined by the so-called Delaunay triangulation (Edelsbrunner, 2001), which creates a unique mesh of triangles. Worth mentioning is that the same material particles are tracked through-out the entire deformation process.

6.3. Parameter estimation from dynamic tests – the inverse problem

The material model parameter estimation is carried out through the solution of an inverse problem (Tarantola, 1987). The direct problem is the finite element problem, which can be posed by considering two sets: the parameter space $\mathscr{P}$ and the solution in space and time $\mathscr{D}$. The solution of the direct problem depends on the input data used for the FE solution, i.e. in general terms the material parameters $\lambda_i \in \mathscr{P}$ give the solution such as

$$\lambda_i \mapsto d_j(\lambda_i) \tag{5}$$

where $d_j \in \mathscr{D}$ are computed responses from the FE model, e.g. displacements and strains. Since the direct problem is nonlinear every element of $\mathscr{D}$ is the image of at least one element of $\mathscr{P}$. The reference data forms

another set $\mathscr{M}$, which is the measured experiment response in space and time. The aim is to estimate the material parameters such that $\mathscr{D}$ matches $\mathscr{M}$. Generally no perfect match exists between $\mathscr{D}$ and $\mathscr{M}$ due to imperfections in the model and inaccuracies in the experiment. Furthermore, because of the nonlinear nature of the direct problem there is no unique inverse solution to the direct problem (Mahnken and Stein, 1994; Tarantola, 1987). These complications are handled by means of minimising the difference between the computed and measured responses with respect to the desired material model parameters. In this specific case, this corresponds to finding the viscoplastic parameter C in the Johnson–Cook material model according to the following optimisation problem:

$$\min_{C\in\mathbb{R}^1} \Phi(C) \tag{6}$$

subjected to

$$C \geqslant 0$$

where $\Phi(C)$ is one of the following objective functions:

$$\Phi_1 = \frac{1}{2N-1}\sum_{m=1}^{M}\sum_{n=1}^{N_m}\frac{[u_n^{\exp}(t_m)-u_n^{\mathrm{FE}}(t_m)]^2+[v_n^{\exp}(t_m)-v_n^{\mathrm{FE}}(t_m)]^2}{s_{un}^2(t_m)} \tag{7}$$

$$\Phi_2 = \frac{1}{2N-1}\sum_{m=1}^{M}\sum_{n=1}^{N_m}\frac{[\varepsilon_{x_n}^{\exp}(t_m)-\varepsilon_{x_n}^{\mathrm{FE}}(t_m)]^2+[\varepsilon_{y_n}^{\exp}(t_m)-\varepsilon_{y_n}^{\mathrm{FE}}(t_m)]^2}{s_{\varepsilon n}^2(t_m)} \tag{8}$$

$$N = \sum_{m=1}^{M} N_m$$

The influence of individual evaluation points $(1,\ldots,N_m)$ is weighted by the estimated uncertainty $s_{un}(t_m)$ or $s_{\varepsilon n}(t_m)$. The displacement and strain quantities are evaluated at a sequence of time instants t_m. A double sum is therefore necessary to cover all points in space and time. The total number of terms in the square sum is $2N$. As shown in Eqs. (7) and (8) two different objective functions are used, one with only strain components and one with only displacement components.

The least-square functional is used as the objective function in the current parameter estimation. The least-square criterion is justified based on the hypothesis that the sum of several different contributions will tend to be normally distributed, irrespective of the probability distribution of the individual contributions. This is often the case e.g. for measurement errors in the long run (Box et al., 1978). There are two conceptually different types of distributions, that of the actual phenomena in the specimens to be measured and that of the random measurement errors. However, it is important to be careful in using the least-square criterion in situations when a small number of large, uncontrolled errors are present in the data. The weighted least-square method is used here to account for the information about the uncertainties in experimental data. Some of the experimental values are known to be more reliable than others. Hence, those values are accordingly assigned larger weight factors.

6.4. Optimisation method

A tailor-made programming system is used for the analysis of the inverse problem (Wikman and Bergman, 2000). The core of the programming system is the optimisation algorithm. Here the unconstrained subspace-searching simplex (subplex) method is used (Rowan, 1990). It is a polytope method designed to locate minima, through so-called direct searching. That is, the value of the objective function is sequentially evaluated and compared in order to find minima without requiring analytically or numerically estimated derivatives of the function. The subplex method is an improvement of the classic Nelder–Mead simplex method and the approach is to decompose the problem into low-dimensional subspaces that the simplex method can search efficiently.

Constraints must be regarded in order to keep the solution in the feasible region of the parameter space. The constraints considered here are so-called side constraints, i.e. direct limitations on the parameter values.

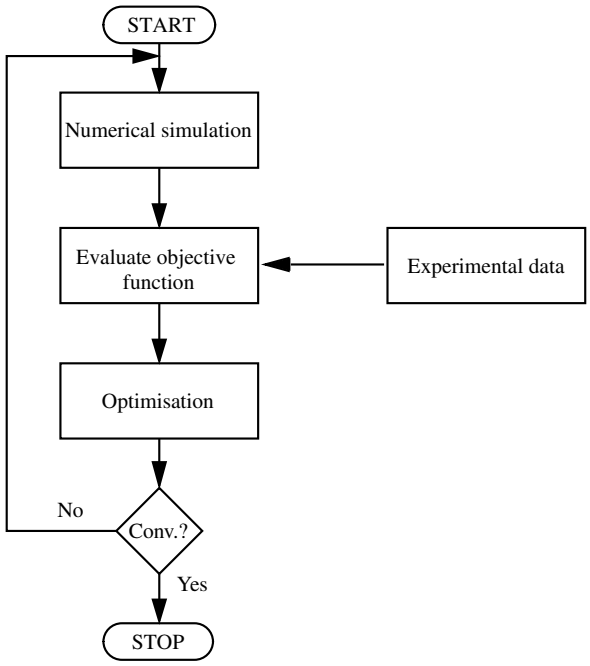

Fig. 8. Principles of an inverse problem.

The constrained problem is formulated as a sequence of unconstrained problems by adding a penalty function to the objective function (Moe, 1973). This approach is based on the fact that the applied optimisation method is found to be insensitive to noisy and non-smooth objective functions.

The scheme from start to stop of an inverse problem is described in Fig. 8. The procedure ends when the pre-defined convergence criteria, such as the tolerance on the variation of the parameters, are satisfied. The tolerance is set to 10^{-3} in this study.

7. Statistical considerations

The objective function, as previously described, is the function whose extreme value is sought for in the feasible region of the parameter space. The parameters are estimated by two optimisation problems, one minimising the difference between the predictions of the strain hardening part of the Johnson–Cook model and static compression test data in a least square sense. The second optimisation problem is based on minimising the least-square difference in the predicted response of the numerical model of the dynamic experiment and actual experimental data from the high strain-rate tests.

7.1. Existence

The necessary requirement for a minimum is that the gradient of the objective function is a zero vector. This comes from the observation that along any line through the minimum, the objective function has both zero slope and positive curvature. Curvature is expressed in terms of the second derivatives of the function or the Hessian. The sufficient requirement thus becomes that the Hessian matrix must be positive definite.

7.2. Stability analysis

The linear system $\mathbf{Ax} = \mathbf{b}$ has a unique solution for every right-hand side only if $\mathbf{A}$ is square and non-singular. The condition number of $\mathbf{A}$ indicates the maximum effect of perturbations in $\mathbf{b}$ or $\mathbf{A}$ on the exact solution of the system. If the condition number is large, the exact solution may be changed substantially by even

small changes in the data. For Newton methods, **A** corresponds to the Hessian matrix **H**, **x** is the search direction and **b** is the gradient vector. The condition number for **H** is given by

$$\kappa(\mathbf{H}) = \|\mathbf{H}\|_2 \|\mathbf{H}^{-1}\|_2 \tag{9}$$

7.3. Confidence intervals

Because the measurement data $\mathscr{M}$ contain random errors, the estimated parameters are not the unique or true set of parameters. The least-squares fitting of data is a maximum likelihood estimation of the fitted parameters if the measurement errors are independent and normally distributed. It is common practice to summarise the distribution of errors in the estimated parameters in the form of a confidence interval. That is, an interval for which one can assert with a given probability, in this case 95%, that it will contain the parameters it is intended to estimate. Assume that λ_i^{opt} is a set of optimal parameters to an objective function Φ. It is then possible to give the 95% confidence interval of the parameters according to

$$\begin{aligned} &\text{Prob}(\lambda_i^{\text{opt}} \in I) \geqslant 0.95 \\ &I = \left[\lambda_i^{\text{opt}} - 1.96\sqrt{V_{ii}}, \lambda_i^{\text{opt}} + 1.96\sqrt{V_{ii}}\right] \\ &V_{ij} = \frac{[G_{ij}(\lambda^{\text{opt}})]^{-1}\Phi(\lambda^{\text{opt}})}{v} \end{aligned} \tag{10}$$

where **V** is the covariance matrix (Fletcher, 1980) and v is the number of degrees of freedom. Note, that repeated indices do not indicate summation. Here, the Gauss–Newton matrix **G** is used as a first order approximation of the Hessian matrix **H**. The matrix **G** (Fletcher, 1980) in its most simple form is given by

$$G_{ij} = 2\sum_{k=1}^{K} \frac{\partial d_k}{\partial \lambda_i}\frac{\partial d_k}{\partial \lambda_j}$$

where d_k are computed quantities and λ_i are the parameters. In order to apply **G** in the second optimisation problem, the quantities have to be identified and the expression must be slightly modified. The computed quantities are the FE-calculated displacements u^{FE} and v^{FE} for objective function Φ_1, and $\varepsilon_x^{\text{FE}}$ and $\varepsilon_y^{\text{FE}}$ for Φ_2. The derivation of **G** based on Φ_2 are described herein. The objective function is weighted by the square of the uncertainties of the measured quantities and thus the expression above is divided with $s_{\varepsilon n}^2(t_m)$ [see Eq. (8)]. Finally, the number of degrees of freedom is included in the objective function and the expression is therefore divided with $2N-1$. Since only one parameter C is used the Gauss–Newton matrix, i.e. Gauss–Newton value, is as follows:

$$G_{11} = \frac{1}{2N-1}\sum_{m=1}^{M}\sum_{n=1}^{N_m}\frac{1}{s_{\varepsilon n}^2(t_m)}\left[\left(\frac{\partial \varepsilon_{x_n}^{\text{FE}}(t_m)}{\partial C}\right)^2 + \left(\frac{\partial \varepsilon_{y_n}^{\text{FE}}(t_m)}{\partial C}\right)^2\right] \tag{11}$$

The Gauss–Newton value based on objective function Φ_1 is derived by replacing the strain quantities and their uncertainties with the displacement quantities with corresponding uncertainties.

According to Eq. (11) G_{11} still contain derivatives, which have to be determined. Approximations are given by

$$\frac{\partial \varepsilon_{x_n}^{\text{FE}}}{\partial C} \approx \frac{\Delta \varepsilon_{x_n}^{\text{FE}}}{\Delta C} \qquad \frac{\partial \varepsilon_{y_n}^{\text{FE}}}{\partial C} \approx \frac{\Delta \varepsilon_{y_n}^{\text{FE}}}{\Delta C} \tag{12}$$

7.4. Goodness-of-fit

An essential question is, how good does the model, with its optimal parameters, fit the experimental data? In order to answer that question, statistical measures of goodness-of-fit are used. Two common measures are the R^2-value and the χ^2-probability (Kleinbaum and Kupper, 1978).

The R^2-value provides a fraction between 0.0 and 1.0, and has no unit. Higher values indicate that the model fits the data better. When R^2 equals 0.0, the best-fit is no better than the mean value of the experimental data. The calculation of R^2 is given by

$$R^2 = 1 - \frac{\mathrm{SS}_{\mathrm{model}}}{\mathrm{SS}_{\mathrm{mean}}}$$

where $\mathrm{SS}_{\mathrm{model}}$ is the sum of squares of the residuals based on the best-fit computed response and the experimental data. Further, $\mathrm{SS}_{\mathrm{mean}}$ is the sum of squares of the differences of the experimental data and its mean value.

Since the variances of the experimentally determined quantities are known and assumed to be normally distributed the so-called χ^2-test can be performed. The objective functions according to Eqs. (7) and (8) have forms suited for the χ^2-test. The χ^2-test can be assigned to each objective function, respectively.

The χ^2-test checks the hypothesis that observations correspond to a certain distribution with its variance. In this case the squared residuals in the nominators in Eqs. (7) and (8) represent the observations and they are checked if they are normal distributed with variances $s^2_{un}(t_m)$ and $s^2_{\dot{\varepsilon}n}(t_m)$, respectively. The significance for the hypothesis is given by the χ^2-distribution. A rule of thumb is that a "typical" value of χ^2 for a "moderately" good fit is approximately equal to one.

8. Results and discussion

The experimental results from the static compression tests are shown in Fig. 9, where the fitted curves according to the strain hardening factor $A + B\bar{\varepsilon}^n_{\mathrm{ep}}$ in the Johnson–Cook model are plotted as dashed lines. The strain hardening parameters are presented in Table 3.

The parameter C, which controls the viscoplastic behaviour is determined for each specimen. The results from the inverse modelling for the two objective functions are presented in Table 4. Since the estimated measurement uncertainties bias the objective functions the more accurate displacements compared to the strains lead to much higher objective function values for Φ_1 than for Φ_2.

In the first optimisation problem for estimation of the strain hardening parameters, both the feasible parameter set $\mathscr{P}$ and the objective function are found to be convex (see Fig. 10). It can be shown that a local

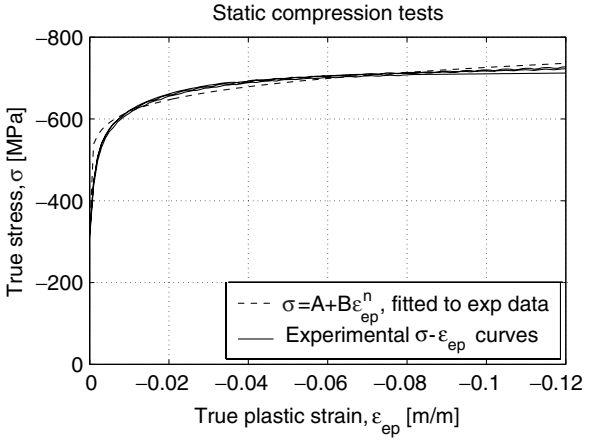

Fig. 9. Static compression tests.

Table 3
Material parameters evaluated at static condition

Φ [MPa]^2	A [MPa]	B [MPa]	n	$\dot{\varepsilon}_0$ [10^{-3} s^{-1}]
295	319	554	0.135	5.7

Table 4
Objective function values and optimal parameter values of C

Specimen	Φ_1	C [10^{-2}]	Φ_2	C [10^{-2}]
1	49.5	2.50	0.420	3.27
2	18.7	2.51	0.258	2.89
3	28.7	2.54	0.246	3.18
Average value		2.52		3.11

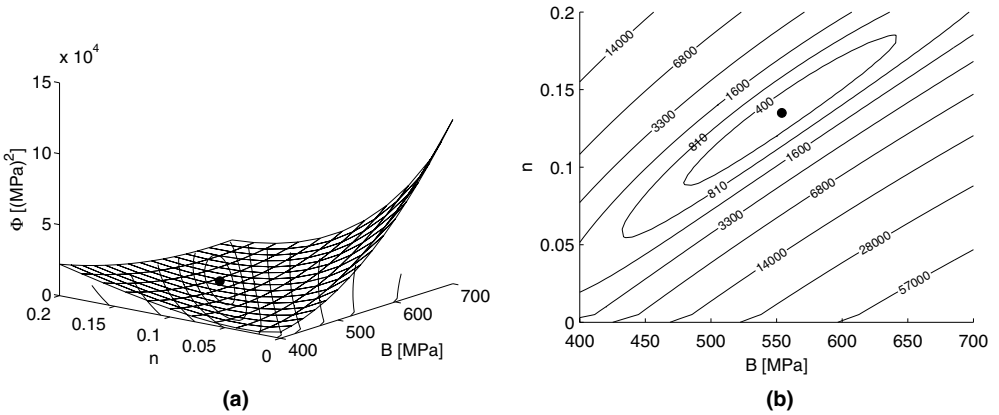

Fig. 10. Objective function values [Eq. (4)] in the region around the minimum, marked as a dot (a). Level curves around the minimum (b).

minimum of a convex function on a convex set is also a global minimum (Arora, 1989). The gradient of the objective function is a zero-vector and the Hessian matrix $\mathbf{H}$ is positive definite at the computed minimum. The Hessian matrix and its first order approximation $\mathbf{G}$, corresponding to the compression tests, computed at the minimum are the following:

$$\mathbf{H} = \begin{pmatrix} 0.806 & -1.55 \times 10^3 \\ -1.55 \times 10^3 & 3.95 \times 10^6 \end{pmatrix}, \qquad \mathbf{G} = \begin{pmatrix} 0.806 & -1.55 \times 10^3 \\ -1.55 \times 10^3 & 3.15 \times 10^6 \end{pmatrix}$$

and its condition number according to Eq. (9) is $\kappa(\mathbf{H}) = 2 \times 10^7$. Hence, the minimum has a tendency of being instable (ill-conditioned), which means that the estimated parameters may be sensitive to small random errors in the data values. Fig. 10 depicts the behaviour of the objective function [Eq. (4)] in the region around the minimum. The minimum is flat and thus the behaviour of the objective function near the minimum solution is rather insensitive to changes in the parameter values. One way to avoid instable minima is to apply some regularisation method (Baumeister, 1987).

In the second optimisation problem, the objective function is not analytically differentiable. Hence, a qualitative evaluation of the minimum is carried out, by plotting function values in a region around the computed minimum solution. Fig. 11(a) show how the parameter C for specimen no. 1 (Φ_2) converges from the start value 2.0×10^{-2} to the final value 3.27×10^{-2} during the optimisation process. In Fig. 11(b) the corresponding objective function value is plotted as function of the parameter value. The plot reveals a convex behaviour of the function around the optimal solution. Little can be said about whether the minimum is local or global because of the FE solution. However, the minimum is found to be stable with respect to parameter C.

The sensitivity δC of parameter C on the von Mises stress $\delta\sigma_e$ in the Johnson–Cook model depends on parameters A, B and n according to

$$\delta\sigma_e|_{A,B,n} = [(A + B\varepsilon_{ep}^n) \ln \dot{\varepsilon}_{ep}^*]\delta C$$

It can be seen that the influence of B and n increases exponentially with strain. This together with the fact that the minimum is relatively flat for finding B and n indicates that the result should be considered with extra care. However, different start values give the same estimated optimal parameters.

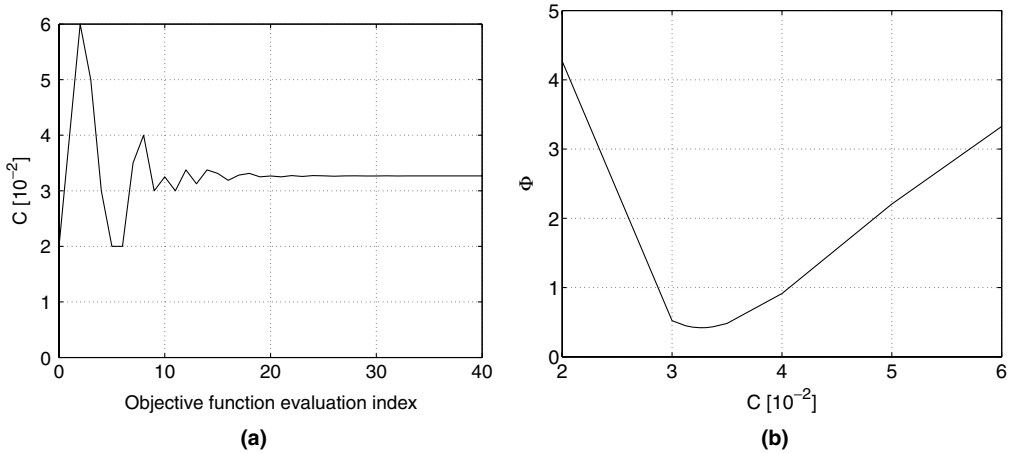

Fig. 11. Development of C from its initial to final (optimal) value (a). Objective function Φ_2 as a function of parameter C (b). The graphs are based on specimen no. 1.

Table 5
Confidence intervals for some estimated parameters

$B \in [552, 556]$ MPa
$n \in [0.134, 0.136]$
$C \in [3.25, 3.29] \times 10^{-2}$

Owing to the total number of estimated parameter values in Tables 3 and 4, the presentation of confidence intervals are limited to the intervals for the strain hardening parameters and the interval for the viscoplastic parameter for specimen no. 1 and objective function Φ_2. Since the parameter A is determined by the offset method, $R_{p0.2}$, and the populations contained only three specimens nothing could be said about their distributions. By using Eq. (10) with the resulting Gauss–Newton matrix $\mathbf{G}$ and the objective function value Φ according to row two in Table 3, the confidence intervals for B and n are estimated. The intervals are presented in Table 5. The confidence interval for C is estimated according to Eqs. (10)–(12), but first the differentials according to Eq. (12) have to be determined. By perturbing the optimal value of C with $\Delta C = [0.025, 0.05, 0.075, 0.1] \times 10^{-2}$ the corresponding finite differences $\Delta\varepsilon_{x_n}^{\mathrm{FE}}$ and $\Delta\varepsilon_{y_n}^{\mathrm{FE}}$ are calculated. By extrapolating these values $\Delta\varepsilon_{x_n}^{\mathrm{FE}}$ and $\Delta\varepsilon_{y_n}^{\mathrm{FE}}$ are approximated for $\Delta C \to 0$. The partial derivatives according to Eq. (12) are then estimated. The resulting confidence interval for C is presented in Table 5.

The quality of the estimation as a whole is measured by the statistical measure called goodness-of-fit. The R^2-value for the two estimation problems is checked. For the B- and n-estimation the R^2-value is computed to 0.84. The R^2-value for the C-estimation reached 0.99 and 0.75, when Φ_1 and Φ_2, respectively are used for specimen no. 1 in the optimisation. This goodness-of-fit control shows an acceptable quality of the performed estimations. An additional goodness test with a more statistical foundation is performed for the C-estimation, according to the χ^2-test. This, however, revealed that the fit is very poor for Φ_1 but good for Φ_2. This is an effect of larger relative errors in the experimental data for the strains. Hence, the model fits statistically better to the data when the standard deviation is greater.

In order to illustrate the coincidence between the experimentally determined quantities and FE-calculated quantities, the strain fields ε_x are presented in Fig. 12 as filled level curves. The fields correspond to specimen no. 1 (Φ_2) and agree acceptable even though there are a few distinctions. First of all the experimental fields are not completely symmetric. Secondly the FE-calculated fields show more distinct peaks in the middle of the fields, whereas the experimental fields appear to have smoother and more uniform distributions of strains. The latter discrepancy might be due to the spatial resolution of the strain fields and the employed filtering technique.

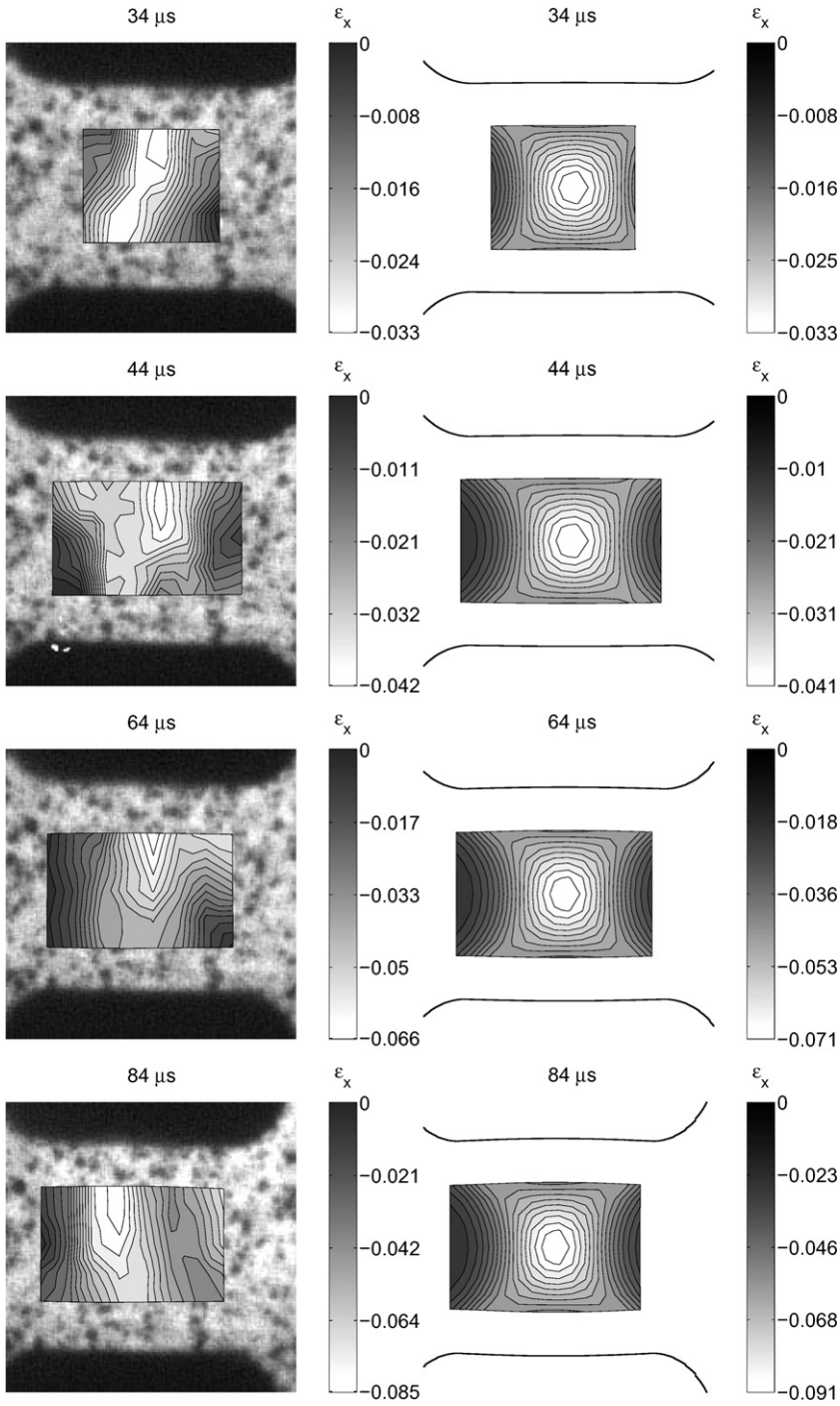

Fig. 12. Strain fields ε_x for specimen no. 1 (Φ_2). The experimentally determined fields are placed to the left. The FE-calculated ones are placed to the right. The time information indicates elapsed time after arrival of the compression wave. Note the different strain scales.

In the split Hopkinson bar experiment the transmitted force is measured in the transmitter bar. As previously mentioned the transmitted force is time-shifted to coincide with the specimen–transmitter bar interface. A similar output force is also evaluated in the FE-simulation and the resulting force $F_{\text{out}}^{\text{FE}}$ is presented in Fig. 5. A comparison between F_{out} and $F_{\text{out}}^{\text{FE}}$ (based on the optimal parameter values) shows a good agreement.

For materials subjected to high strain rates nearly 100% of the plastic work is converted to heat (Kapoor and Nemat-Nasser, 1998). Under the presented experimental circumstances adiabatic conditions prevail. The assumption of no thermal affect, resulting in a cancellation of the thermal factor in the Johnson–Cook model, is checked by performing a FE-calculation based on the estimated material parameters and adiabatic conditions. The FE-calculation showed a temperature increase of approximately 80 K in the region of largest strains. Since the thermal behaviour is not studied for the chosen material the effect of the temperature increase is hard to predict accurately. However, an indication can be provided by using thermal characteristics for other similar materials. For example, most of the characterised steel alloys by Johnson and Cook (1983) achieved a value of approximately 1 for the thermal softening exponent m [see Eq. (2)]. According to the Johnson–Cook model with $m = 1$ a temperature increase of 80 K results in a thermal softening of approximately 5%. Even though, this study resulted in a relatively low decrease of the flow stress, it indicates that the thermal response is of significance.

In the current work, three of four material parameters of the Johnson–Cook model are determined by inverse modelling. However, the suggested method applies also to models containing more parameters. In such cases, the computational work becomes heavier and the existence, uniqueness and stability analysis more severe. The behaviour of the optimisation problem is to a large extent material model dependent. This means that the mathematical structure of the model influences the behaviour of the optimisation problem. For example the covariance of parameters influences the uniqueness of the solution. Hence, the correlation between parameters controls the confidence with which the parameters can be determined (Baumeister, 1987).

Analytical solutions are normally not available for the derivatives and numerical computation of the sensitivities is a necessity. Selecting step sizes in such discretisation procedures is of great importance. Too large steps will generate truncation errors while too short steps cause condition errors (Haftka and Adelman, 1989).

9. Conclusions

A method for viscoplastic parameter estimation, based on high-strain rate experiments and inverse modelling, is presented. In contrast to the presented method, the classic split Hopkinson method requires force equilibrium in the specimen, which in some cases is difficult to achieve, e.g. for soft materials, where the wave propagation speed is low. Further, the Hopkinson bars are not allowed to deform plastically. Thus, the specimen material has to be softer than the bar material. In the presented method, when a nonhomogeneous state of stress (and strain) is allowed, the specimen can be made with a narrow part, which concentrates the high stresses and the bars are prevented from plastic deformation.

The least-square objective functions used for comparing the measured and computed field information show to be useful in this application. The fact that the objective functions contain sums of squares enables use of the Gauss–Newton approximations of the Hessian.

The Delaunay triangulation method for interpolating FE data to the measurement points was straightforward to apply and worked well.

The fact that the uncertainties of the strain measurement are of the same order of magnitude as the measured strains indicates that improvement regarding the speckle measurement is of great interest. With a more modern CCD-detector sharper pictures with higher spatial resolution would probably be captured and higher correlation values should hopefully be obtained. As already mentioned, the obtained speckle size, namely six pixels, is three times larger than the optimum size of two pixels. An optimum size of the speckles would improve the accuracy nine times, i.e. approximately one order of magnitude. Furthermore, since new algorithms for speckle evaluation are continuously under development utilizing other algorithms could be interesting areas to study.

The estimated uncertainties in the experimental data play a crucial role for the calculated goodness-of-fit measure χ^2. Large quantities of data with high accuracy as the measured displacement components increase the requirement of predictive capability of the employed material model. The commonly used Johnson–Cook model shows to be insufficient to describe the measured material behaviour from a statistical point of view when the objective function is based on only the displacement components (Φ_1). A much better fit is obtained when using only the relatively uncertain strain components in the objective function as in Φ_2.

Since the strain-rate distribution in the presented dynamic tests is restricted to magnitude of 10^2–$10^3\ s^{-1}$ experiments in the mid range 10^{-1}–$10^2\ s^{-1}$ have to be performed to obtain material parameters valid for a

wide range of strain rates. Further, a study of the thermal behaviour would increase the reliability of the estimated material parameters. Finally, it seems likely that the method is well suited for characterising of soft and high strength materials and therefore other materials than mild steels would be of interest to study.

Acknowledgements

The authors are grateful to Dr. K.-G. Sundin for his contributions and comments on the manuscript. The ULTRANAC camera purchase was possible due to a grant from the Swedish Council for Planning and Coordination of Research (FRN). The financial support from Complab, *Centre for testing and development of mechanical components*, is gratefully acknowledged.

References

Arora, J.S., 1989. Introduction to Optimum Design. McGraw-Hill, New York, USA.

ASTM Standard E9-89a, 1995. Standard test methods of compression testing of metallic materials at room temperature. Annual book of ASTM standards, vol. 03.01., pp. 97–104.

Baumeister, J., 1987. Stable Solution of Inverse Problems. Braunschweig: Vieweg & Son, Germany.

Box, G.E.P., Hunter, W.G., Hunter, J.S., 1978. Statistics for Experimenters. John Wiley & Sons.

Edelsbrunner, H., 2001. Geometry and Topology for Mesh Generation. Cambridge University Press.

Fletcher, R., 1980. Practical Methods of OptimizationUnconstrained Optimization, vol. 1. John Wiley & Sons.

Follansbee, P.S., Kocks, U.F., 1988. A constitutive description of the deformation of copper based on the use of the mechanical threshold stress as an internal state variable. Acta Metall. 36, 81–93.

Grantham, S.G., Siviour, C.R., Proud, W.G., Walley, S.M., Field, J.E., 2003. Speckle measurements of sample deformation in the split Hopkinsons pressure bar. J. Phys. IV France 110, 405–410.

Gray III, G.T., 2000. Classic split-Hopkinson pressure bar testing. ASM Handbook 8, 462–476.

Haftka, R.T., Adelman, H.M., 1989. Recent developments in structural sensitivity analysis. Struct. Optim. 1, 137–151.

Hopperstad, O.S., Børvik, T., Langseth, M., Labibes, K., Albertini, C., 2003. On the influence of stress triaxiality and strain rate on the behaviour of a structural steel. Part I. Experiments. Eur. J. Mech. A Solids 22, 1–13.

Jernkvist, L.O., Thuvander, F., 2003. Optical method to study material behaviour at high strain rates. In: Ståhle, P., Sundin, K.G. (Eds.), Proceedings of the IUTAM Symposium on Field Analysis for Determination of Material Parameters – Experimental and Numerical Aspects, Abisko National Park, Kiruna, Sweden, July 31 – August 4, 2000. Kluwer Academic Publishers, Dordecht, the Netherlands, pp. 51–61.

Johnson, G.R., Cook, W.H., 1983. A constitutive model and data for metals subjected to large strains, high strain rates and high temperatures. In: Proc. 7th Int. Symp. on Ballistics, The Netherlands, pp. 541–547.

Kajberg, J., Sjödahl, M., 2003. Optical method to study material behaviour at high strain rates. In: Ståhle, P., Sundin, K.G. (Eds.), Proceedings of the IUTAM Symposium on Field Analysis for Determination of Material Parameters – Experimental and Numerical Aspects, Abisko National Park, Kiruna, Sweden, July 31 – August 4, 2000. Kluwer Academic Publishers, Dordecht, the Netherlands, pp. 37–49.

Kajberg, J., Sundin, K.G., Melin, L.G., Ståhle, P., 2004. High strain-rate tensile testing and viscoplastic parameter identification using microscopic high-speed photography. Int. J. Plast. 20, 561–575.

Kajberg, J., Lindkvist, G., 2004. Characterisation of materials subjected to large strains by inverse modelling based on in-plane displacement fields. Int. J. Solids Struct. 41, 3439–3459.

Kapoor, R., Nemat-Nasser, S., 1998. Determination of temperature rise during high strain rate deformation. Mech. Mater. 27, 1–12.

Kleinbaum, D.G., Kupper, L.L., 1978. Applied Regression Analysis and Other Multivariable Methods. Duxbury Press, North Scituate, Massachusetts.

Kolsky, H., 1949. An investigation of the mechanical properties of materials at very high rates of loading. Proc. Phys. Soc. Lond. B 62, 676–700.

Lemaitre, J., Chaboche, J.L., 1990. Mechanics of Solid Materials. Cambridge University Press.

Liang, R., Khan, A.S., 1999. A critical review of experimental results and constitutive models for BCC and FCC metals over a wide range of strain rates and temperatures. Int. J. Plast. 15, 963–980.

Mahnken, R., Stein, E., 1994. The identification of parameters for visco-plastic models via finite-element methods and gradient methods. Modell. Simul. Mater. Sci. Eng. 2, 697–716.

Meyers, M.A., 1994. Dynamic Behaviour of Materials. John Wiley & Sons.

Moe, J., 1973. Penalty-function methods. In: Gallagher, R.H., Zienkiewicz, O.C. (Eds.), Optimum Structural Design, Theory and Applications.

Molin, N.-E., Sjödahl, M., Gren, P., Svanbro, A., 2004. Speckle photography combined with speckle interferometry. Opt. Lasers Eng. 41, 673–686.

Nelder, J.A., Mead, R., 1965. A simplex method for functional minimization. The Computer J. 7, 308–313.

Nemat-Nasser, S., Kapoor, R., 2001. Deformation behavior of tantalum and a tantalum tungsten alloy. Int. J. Plast. 17, 1351–1366.

Perzyna, P., 1963. The constitutive equations for rate-sensitive plastic materials. Quart. Appl. Math. 20, 321–332.
Press, W.H., Teukolsky, S.A., Vetterling, W.T., Flannery, B.P., 1992. Numerical Recipies in C, second ed. Cambridge University Press.
Rowan, T.H., 1990. Functional stability analysis of numerical algorithms. Ph.D. thesis. The University of Texas at Austin, USA.
Sjödahl, M., 1994. Electronic speckle photography: increased accuracy by nonintegral pixel shifting. Appl. Opt. 33, 6667–6673.
Sjödahl, M., 1997. Accuracy in electronic speckle photography. Appl. Opt. 36, 2875–2885.
Sjödahl, M., Benckert, L.R., 1994. Systematic and random errors in electronic speckle photography. Appl. Opt. 33, 7461–7471.
Tarantola, A., 1987. Inverse Problem Theory, Methods for Data Fitting and Model Parameter Estimation. Elsevier Publisher B.V., New York, USA.
Walley, S.M., Field, J.E., 1994. Strain rate sensitivity of polymers in compression from low to high strain rates. Dymat J. 1, 211–227.
Wattrisse, B., Chrysochoos, A., Muracciole, J.-M., Nemoz-Gaillard, M., 2001. Analysis of strain localization during tensile tests by digital image correlation. Exp. Mech. 41, 29–39.
Wikman, B., Bergman, G., 2000. An Inverse Modelling System, User Manual Version 1.0. Technical report 2000:27, Luleå University of Technology, Luleå, Sweden.
Zerilli, F.J., Armstrong, R.W., 1987. Dislocation-mechanics-based constitutive relations for material dynamics calculations. J. Appl. Phys. 61, 1816–1825.